

1 Presence and consequences of co-existing methane gas with  
2 hydrate under two phase water-hydrate stability conditions

3 **Sourav K. Sahoo<sup>1,2\*</sup>, Héctor Marín-Moreno<sup>1</sup>, Laurence J. North<sup>1</sup>, Ismael Falcon-Suarez<sup>1</sup>,**  
4 **Bangalore N. Madhusudhan<sup>3</sup>, Angus I. Best<sup>1</sup> and Tim A. Minshull<sup>2</sup>**

5 *<sup>1</sup>National Oceanography Centre, University of Southampton Waterfront Campus, European*  
6 *Way, Southampton, SO14 3ZH, United Kingdom.*

7 *<sup>2</sup>National Oceanography Centre Southampton, University of Southampton, European Way,*  
8 *Southampton, SO14 3ZH, United Kingdom.*

9 *<sup>3</sup>Faculty of Engineering and the Environment, University of Southampton, Southampton, United*  
10 *Kingdom*

11

12 \*Corresponding Author: Sourav K. Sahoo ([sourav.sahoo@soton.ac.uk](mailto:sourav.sahoo@soton.ac.uk))

13

14 **KEY POINTS**

15 We present a method to calculate continuously saturations of pore phases during hydrate  
16 formation/dissociation from pressure and temperature.

17 In our experiment up to 26% hydrate co-existed with about 12% gas in three hydrate formation  
18 cycles with 10 and 55 MPa differential pressure

19 We suggest the dominant mechanism for gas and hydrate co-existence in our experiment is  
20 formation of hydrate-enveloped gas bubbles.

21

22 **ABSTRACT**

23 Methane hydrate saturation estimates from remote geophysical data and borehole logs are needed  
24 to assess the role of hydrates in climate change, continental slope stability, and energy resource  
25 potential. Here, we present laboratory hydrate formation/dissociation experiments in which we  
26 determined the methane hydrate content independently from pore pressure and temperature, and  
27 from electrical resistivity. Using these laboratory experiments, we demonstrate that hydrate  
28 formation does not take up all the methane gas or water even if the system is under two phase  
29 water-hydrate stability conditions and gas is well distributed in the sample. The experiment  
30 started with methane gas and water saturations of 16.5% and 83.5% respectively; during the  
31 experiment, hydrate saturation proceeded up to 26% along with 12% gas and 62% water  
32 remaining in the system. The co-existence of hydrate and gas is one possible explanation for  
33 discrepancies between estimates of hydrate saturation from electrical and acoustic methods. We  
34 suggest that an important mechanism for this co-existence is the formation of a hydrate film  
35 enveloping methane gas bubbles, trapping the remaining gas inside.

36

## 37 **1 INTRODUCTION**

38 Hydrate is a naturally occurring ice-like, crystalline solid comprising a hydrogen-bonded  
39 water lattice with trapped gas molecules, that forms in seafloor sediments at high pressures and  
40 low temperatures (Kvenvolden, 1993). Nearly all the gas in natural hydrates is methane, with the  
41 remainder comprising higher order hydrocarbons such as ethane (Kvenvolden, 1993). Remote  
42 geophysical methods are used to quantify seafloor methane hydrates over broad areas. Typically  
43 these methods exploit the increase in seismic velocity (e.g., Fohrmann & Pecher, 2012; Lee &  
44 Collett, 2006b; Schnurle et al., 2004) and electrical resistivity (e.g., Hsu et al., 2014;  
45 Schwalenberg et al., 2010; Weitemeyer et al., 2006) caused when hydrate replaces saline water  
46 in sediment pores. However, accurate quantification of methane hydrate saturation is hampered  
47 by uncertainties in the relationship between these parameters and hydrate content (e.g., Goswami  
48 et al., 2015; Hsu et al., 2014; Lee & Collett, 2008; Schnurle et al., 2004).

49 Sub-seabed electrical resistivity can be measured using borehole logging (e.g., Miyakawa  
50 et al., 2014) or marine controlled source electromagnetic (CSEM) methods (e.g., Weitemeyer et  
51 al., 2006). Some field locations show discrepancies between hydrate saturations derived from  
52 resistivity and seismic/sonic methods (Table 1). This difference is a potential source of  
53 uncertainty in estimates from geophysical data of the carbon inventory stored in hydrate and in  
54 resulting assessments of well stability and methane production from hydrate reservoirs.

55 Hydrate content is often estimated from the increase in electrical resistivity compared to  
56 background sediments with no hydrates (e.g., Weitemeyer et al., 2006; Lee and Collett, 2008;  
57 Schwalenberg et al., 2010; Hsu et al., 2014). However, this method does not differentiate  
58 between gas and hydrate because both have higher resistivity than conductive pore fluid (e.g.,  
59 Lee and Collett, 2008). Hereafter, the term gas is used to describe methane that is not stored in

60 hydrate or dissolved in water, and may be mobile or immobile. In seismic data, gas and hydrate  
61 have been identified from a decrease and increase in P-wave velocity, respectively (e.g., Guerin  
62 et al., 1999; Schnurle et al., 2004; Lee and Collett, 2006; Fohrmann and Pecher, 2012). Because  
63 of their strong effect on P wave velocity (White, 1977), the presence of even small amounts of  
64 gas can obscure any increase in velocity caused by the presence of hydrate. In this case, estimates  
65 of hydrate content based on P wave velocity may differ significantly from those based on  
66 resistivity.

67         The presence of co-existing hydrate and gas within the gas hydrate stability zone (GHSZ)  
68 has been inferred in several locations away from seabed methane plumes (e.g., Guerin et al.,  
69 1999; Milkov et al., 2004; Lee and Collett, 2006; Miyakawa et al., 2014). Such field studies have  
70 attributed this presence of gas within the GHSZ to: (i) influx of gas into the GHSZ along  
71 fracture/faults (Gorman et al., 2002; Lee & Collett, 2006b; Smith et al., 2014); (ii) local  
72 deviations from two phase water-hydrate stability conditions (pressure-temperature-salinity)  
73 resulting in local hydrate dissociation within the GHSZ (Guerin et al., 1999; Milkov et al., 2004);  
74 or (iii) hydrate formation kinetics (Torres et al., 2004). Drilling activities may also dissociate  
75 hydrates around a well, releasing gas within the GHSZ (Lee & Collett, 2006b).

76         At Site 1245 of ODP Leg 204, the amount of gas within the GHSZ was inferred  
77 independently from NMR logs and sonic velocity logs, with four times less gas inferred from  
78 sonic logs than from NMR logs (Lee & Collett, 2006b). In the Kumano basin, Nankai Trough,  
79 offshore Japan, the presence of co-existing gas within the GHSZ was inferred from velocity and  
80 resistivity logs: in certain parts of the well, velocity decreased with no corresponding decrease in  
81 resistivity, probably due to the presence of gas (Miyakawa et al., 2014). In both these locations,  
82 transport of gas into the GHSZ along faults or local hydrate dissociation during drilling has been

83 inferred (Lee & Collett, 2006b; Miyakawa et al., 2014). Milkov et al. (2004) explained the  
84 presence of gas within the GHSZ at Site 1249 of ODP Leg 204 by high residual pore water  
85 salinity, that limited further hydrate formation (Hesse & Harrison, 1981; Liu & Flemings, 2006;  
86 Milkov et al., 2004). At Site 995 of ODP Leg 164, co-existing gas and hydrate in the base of the  
87 GHSZ have been explained by hydrate dissociation in smaller pores because of capillary effects  
88 along with hydrate stability in bigger pores (Guerin et al., 1999). Elsewhere, several locations do  
89 not show any evidence of co-existing hydrate and gas within the GHSZ (e.g., Fujii et al., 2015).

90         However, gas can also be present in two phase water-hydrate stability conditions due to  
91 two mechanisms. Firstly, hydrate can contain inclusions of gas (Schicks et al., 2006), which  
92 could either be connected or disconnected to the pore network. Disconnected inclusions  
93 (occlusions) could remain in the hydrate or could also be a pre-hydrate phase, where hydrate  
94 formation is still in process (Schicks et al., 2006). Occlusions of gas may be removed over time  
95 by diffusion, but in a dynamic pore fluid system with gas production, diffusion is unlikely to  
96 dominate due to its relatively slow rate (Milkov et al., 2004; Suess et al., 2001). Secondly,  
97 hydrate formation can block contacts between gas and water within sediment pores, and form  
98 pockets of gas (which could include several pores) (e.g. Chaouachi et al., 2015; Yang et al.,  
99 2016). Kinetic modelling of hydrate formation and dissociation in porous media suggests that it  
100 is highly unlikely that hydrate can achieve true equilibrium because there are too many phases in  
101 the system (e.g., Vafaei et al., 2014). Therefore, the limiting phase (methane in excess water  
102 conditions; water in excess gas conditions) is unlikely to be completely used up to form hydrates  
103 even if two phase water-hydrate stability conditions prevail.

104         Here, we present results from a laboratory experiment of methane hydrate formation and  
105 dissociation in Berea sandstone. We calculated continuously the evolution of the brine, gas and

106 hydrate saturations during hydrate formation and dissociation from pore pressure and  
107 temperature. Our calculation method does not assume that hydrate formation continues until the  
108 limiting phase is exhausted, and we show that about 12% gas co-exists with 26% hydrate under  
109 pressure, temperature and salinity conditions favorable for more hydrate formation.

110

## 111 **2 HYDRATE FORMATION AND DISSOCIATION EXPERIMENTS**

112 We conducted laboratory experiments involving repeated cycles of methane hydrate  
113 formation and dissociation inside a high-pressure cell under excess water conditions.

114

### 115 **2.1 Sample properties and experimental setup**

116 For the test, we selected a 2 cm height, 5 cm diameter core sample of Berea sandstone.  
117 The porosity was 0.22 and the absolute permeability was 448 mD ( $\sim 4.5 \times 10^{-13} \text{ m}^2$ ) at  
118 atmospheric conditions. The permeability was measured with (gas) permeameter and the porosity  
119 with a pycnometer.

120 The experiment was conducted in a stainless steel triaxial cell core holder, designed to  
121 host and pressurize 5 cm diameter rock samples up to 65 MPa of confining and pore pressure  
122 (Figure 1), and instrumented to monitor temperature (both sample and ambient) (M. H. Ellis,  
123 2008). The inner sleeve that prevents the direct contact between the mineral oil used as confining  
124 fluid and the rock sample is perforated by 16 electrodes coupled to a data acquisition system.  
125 Under typical operating conditions the relative error in resistivity measurement is  $< 0.1\%$  (at  
126 frequencies 1 - 500 Hz) for homogenous and isotropic samples in the electrical resistivity range  
127 1-100  $\Omega \text{ m}$  (North et al., 2013). Axially, perspex buffer rods electrically isolate the sample from  
128 the cell. The inner temperature sensor was placed on the outer side-wall of the sleeve at the

129 sample height, to provide accurate monitoring of the sample temperature. The pore fluid pipe  
130 line is connected to (i) a pumping-syringe containing a 35 g/L NaCl solution in deionized-  
131 deaerated water, (ii) a vacuum pump and (iii) a CH<sub>4</sub>-bottle pressurized at 12 MPa (see Figure 1).

132

## 133 **2.2 Method of hydrate formation**

134 We followed the method of Waite et al. (2004) with an initial brine saturation of 83.5%  
135 which allowed an excess water condition (M. H. Ellis, 2008; Priest et al., 2009). Our hydrate  
136 formation method and experimental set up represent gas hydrate systems where localized gas  
137 reaches the base of the GHSZ.

138 The sample was firstly oven-dried at 60°C, placed in the high pressure triaxial cell  
139 (Figure 1), then a hydrostatic confining pressure of 10 MPa was applied externally to the sample.  
140 A vacuum up to 1 Pa was applied internally to the sample to remove air from the pore space. The  
141 presence of air affects the saturation calculation and also some gases present in the air, such as  
142 CO<sub>2</sub>, can form hydrate. A volume of brine (comprising 35 g/L NaCl solution in deionized and  
143 deaerated water) was injected through the pore fluid line into the Berea rock sample using a  
144 syringe pump, calculated to fill 83.5% of the pore space. Hence, the sample was only partially  
145 filled with brine, with the remaining pore space available for subsequent methane gas injection  
146 (e.g., Waite et al., 2004; Winters et al., 2004). We left the sample for three days so that the pore  
147 fluids could re-distribute throughout the sample by capillary forces. The remaining pore space  
148 (16.5%), which was previously under vacuum, may have been occupied by water vapor and/or  
149 remaining air.

150 Methane gas was then injected to achieve a pore fluid pressure of 11.9 MPa (Figure 2),  
151 and, simultaneously, the confining pressure was increased to 21.9 MPa to maintain a constant

152 differential pressure of 10 MPa during the whole experiment. The pore fluid system was sealed,  
153 keeping the reservoir between the sample and valve  $V_A$  (Figure 1) filled with methane gas, which  
154 is free to move in and out of the sample as a result of potential pore pressure variations. Finally,  
155 four cycles of hydrate formation/dissociation were triggered by cooling/heating the setup in a  
156 controlled manner, i.e., in and out from the gas hydrate stability conditions (GHSC).

157         The cooling of the system into the GHSC, to a set temperature of  $5^\circ\text{C}$ , generated a reduction  
158 in pore pressure (Figure 2) that can be explained mainly by hydrate formation, with some  
159 contribution from methane gas contraction and increased gas solubility. The pressure reduction  
160 appears to take place in two stages (Figure 2). On trajectory A-B the system is cooled rapidly (in  
161 5.5 hours). Here, the pressure drops due both to cooling and to hydrate formation. On trajectory  
162 B-C the temperature remains around  $5^\circ\text{C}$  and only the pressure drops. Here, the pressure drop is  
163 mainly due to hydrate formation and takes much longer (73 hours) than on trajectory A-B. The  
164 formation of hydrate also generates a slight increase in temperature caused by exothermic hydrate  
165 formation (Hwang et al., 1990). This increase is very clear on trajectory B-C. On trajectory A-B,  
166 at around 201.4 h, there is a sudden pore fluid pressure and temperature increase (Figure 2). This  
167 pressure increase is likely due to the interplay between the cooling of the system and the  
168 exothermic effect of hydrate formation. Cooling and the consumption of pore fluids due to hydrate  
169 formation both lead to a decrease in pressure. However, hydrate formation also leads to an increase  
170 in temperature, which can result in a slight increase in pressure (Figure 2c and d). The net effect  
171 depends on the balance between the rate of cooling and the rate of hydrate formation. Once hydrate  
172 formation ceased, indicated by the end of the pore pressure decrease (point C in Figure 2), the  
173 system was left at that pressure and temperature for several hours to ensure maximum hydrate

174 formation, evidenced by the horizontal asymptotic behavior of the pore pressure (Figure 2b) and  
175 of the saturation lines for each cycle (Figure 3).

176 Hydrate dissociation was initiated by increasing the temperature above the GHSC to room  
177 temperature. We also did a separate experiment under identical conditions in which we left the  
178 sample under hydrate stability conditions at 5°C (point C in Figure 2a) for 1 month and saw that  
179 maximum saturation of methane hydrate occurred in the first 75 hours. This experiment also  
180 resulted in 22% hydrate saturation. The differential pressure was held at 10 MPa in the first and  
181 second cycles of hydrate formation and dissociation, and then increased to 55 MPa for the third  
182 and fourth cycles. This was done to explore the effects of micro-cracks on acoustic properties  
183 (included in future work) that are generally open at lower differential pressures (10 MPa) and  
184 closed at higher pressures (55MPa), based on previous resistivity and ultrasound data for Berea  
185 (Han et al., 2011). The initial pore fluid pressure for the third cycle was 11.98 MPa (0.08 MPa  
186 above that for the first cycle).

### 187 **3 SATURATION CALCULATIONS**

188 We tracked the evolution of the saturations of gas, brine and hydrate from the changes in  
189 pore fluid pressure and temperature using the real gas equation (the PT method), and  
190 independently from electrical resistivity measurements (the ERT method).

#### 191 **3.1 PT method**

192 We calculated continuously the saturations of the three phases (gas, brine, hydrate) from  
193 the changes in pore fluid pressure and temperature using the real gas equation. These  
194 measurements were recorded at one minute intervals during the experiment. This method does  
195 not assume that hydrate formation continues until the limiting phase is exhausted (e.g., Sultaniya

196 et al., 2015) nor that coexistence occurs only under three-phase stability conditions (e.g., You et  
197 al., 2015). This allows us to deduce the physical processes that occur throughout the cycle of  
198 hydrate formation and dissociation.

199 Our method assumes a closed system and conservation of the molar mass of methane and  
200 water in the sample pore space. Methane can be present in hydrate, dissolved in brine or as gas.  
201 Water can be present as liquid in the pore space (brine) or in hydrate (pure water). The pore  
202 volume in the sample and inner volume of the input gas pipe were measured before starting the  
203 experiment, and were assumed to remain constant throughout the experiment. A change in  
204 effective pressure can change the sample's pore volume, but for the magnitude of the dynamic  
205 stresses applied, this change is negligible (< 0.3% for Berea sandstone) (Rutter & Glover, 2012).  
206 A change in temperature can also change the sample's pore volume. Such changes are likely to  
207 be negligible in our experimental range (5 - 22 °C) as the volumetric thermal expansion  
208 coefficient of sandstone is about  $3 \times 10^{-5}$  per °C in the temperature range 20 - 100 °C (Skinner,  
209 1966). So we assumed the volume of the input gas pipe remains constant because it is always at  
210 ambient pressure and the ambient temperature was controlled to  $20 \pm 2$  °C. The pores of the  
211 Berea sandstone can be occupied by gas, water or hydrate. Hydrate can only form in the pore  
212 space of the sample and no hydrate forms in the gas input pipe because it is outside hydrate  
213 stability conditions.

214 The non-ideal gas law is:

$$p V = n R T Z \quad (1)$$

215 where  $p$  is gas pressure,  $V$  is volume,  $n$  is the number of moles of methane gas,  $R$  is the  
216 universal gas constant and  $T$  is temperature.  $Z$  is an empirical compressibility factor calculated  
217 using the Peng–Robinson equation of state (Peng & Robinson, 1976), and varies with

218 temperature and pressure. Initially there was no hydrate in the sample. The sample pore volume  
 219  $V_{ts}$  was independently measured with a pycnometer, and a known volume of water  $V_{w0}$ ,  
 220 measured using a syringe pump, was injected into the sample. The initial number of moles of  
 221 water is given by

$$n_{w0} = \frac{V_{w0} D_{w0}}{M_w} \quad (2)$$

222 where  $D_{w0}$  is the density of brine at 35 g/L salinity and  $M_w$  is the molar mass of this brine. For  
 223 the pipe, from eq. 1 we have

$$p_0 V_p = n_{p0} R T_{p0} Z_{p0} \quad (3)$$

224 where  $p_0$  is initial gas pressure, which is the same in both the sample and the pipe,  $V_p$  is the  
 225 volume inside the pipe,  $n_{p0}$  is the initial number of moles of methane gas in the pipe,  $T_{p0}$  is the  
 226 temperature in the pipe, and  $Z_{p0}$  is the compressibility factor of methane under the initial pipe P-  
 227 T conditions.

228 For the sample, eq. 1 gives

$$p_0 V_{ms0} = n_{s0} R T_{s0} Z_{s0} , \quad (4)$$

$$V_{ms0} = V_{ts} - V_{w0} , \quad (5)$$

229 where  $V_{ms0}$  is the initial volume of methane gas in the sample,  $n_{s0}$  is the initial number of moles  
 230 of methane gas in the sample,  $T_{s0}$  is the initial temperature of the sample, and  $Z_{s0}$  is the  
 231 compressibility factor of methane under the initial sample P-T conditions. In our method, we  
 232 accounted for the dependency of methane solubility in water, denoted by  $b$ , on temperature and  
 233 salinity (Tishchenko et al., 2005) and that of hydrate and brine densities on pressure and  
 234 temperature (Lu & Sultan, 2008; Millero et al., 1980) using the equation:

$$n_{sw0} = V_{w0} D_{w0} b_0, \quad (6)$$

235 where  $n_{sw0}$  is the initial number of moles of methane in solution and  $b_0$  is the initial solubility.

236 The total number of moles of methane in the system  $n_t$  was therefore

$$n_t = n_{p0} + n_{s0} + n_{sw0}. \quad (7)$$

237 Once the temperature decreases below that for hydrate stability, hydrate starts to form  
 238 from the methane and water in the sample's pore space. This process reduces the sample's gas  
 239 pressure, generating an inflow of methane gas from the pipe to regain equilibrium of pore fluid  
 240 pressure. The net result is an overall decrease in the gas pressure. From this new gas pressure and  
 241 the pipe and sample temperatures,  $T_p$  and  $T_s$ , we can calculate the number of methane moles in  
 242 each phase. For a gas pressure  $p$

$$V_h = n_h \frac{M_h}{D_h}, \quad (8)$$

$$V_w = (n_{w0} - n_h \cdot c) \frac{M_w}{D_w}, \quad (9)$$

$$V_{ms} = V_{ts} - V_w - V_h, \quad (10)$$

$$p V_p = n_p R T_p Z_p, \quad (11)$$

$$p V_{ms} = n_s R T_s Z_s, \quad (12)$$

$$n_{sw} = V_w D_w b, \quad (13)$$

243

244 where  $V_h$  is the volume of hydrate,  $n_h$  is the number of moles of hydrate,  $M_h$  is the molecular

245 mass of hydrate,  $D_h$  is the density of hydrate and  $c$  is the hydration number (i.e., the number of

246 water molecules required to form hydrate per molecule of methane). The total number of moles  
 247 of methane in the system remains constant, so  $n_h$  can be obtained from

$$n_h = n_t - n_p - n_s - n_{sw}. \quad (14)$$

248 The hydrate saturation is given by

$$S_h = \frac{V_h}{V_{ts}}. \quad (15)$$

249 Combining equation 8-15, we obtain:

250

$$S_h \quad (16)$$

$$= \frac{\left( \frac{p_0 V_{p0}}{R T_{p0} Z_{p0}} + \frac{p_0 (V_{ts} - V_{w0})}{R T_{s0} Z_{s0}} + V_{w0} D_{w0} b_0 - \frac{p V_p}{R T_p Z_p} - \frac{p V_s}{R T_s Z_s} - V_w D_w b \right) \frac{M_h}{D_h}}{V_{ts}}.$$

251

252 All the symbols defined in this section are listed in Table 2 and constants are listed in Table 3.

253

### 254 3.2 ERT method

255 We estimated the saturation of resistive material in the pore space from measured bulk  
 256 resistivity of the sample. As both hydrate and gas are resistive compared to the conductive brine,  
 257 it is not possible to obtain the individual saturations of gas and hydrate separately by this approach.

258 To determine this saturation, the first step is to calculate the saturation of brine. Several  
 259 approaches can be used to estimate the saturation of brine from measured electrical resistivity (e.g.,

260 Archie, 1942; Bussian, 1983; Glover, 2010; de Lima & Sharma, 1990; Revil et al., 1998;

261 Simandoux, 1963; Waxman & Smits, 1968). This interpretation is complicated in the presence of  
 262 clay minerals as they have charge deficiency. The ‘counter ions’ required to balance this charge  
 263 deficiency are in the double layer. These counter ions can move along the grain water surface  
 264 under the influence of an external electric field. Hence, the macroscopic electrical conduction in a  
 265 saturated/partially saturated porous medium with clay can be via a) bulk conduction caused by the  
 266 movement of ions of the conducting pore fluid, and b) surface conduction in the vicinity of the  
 267 fluid/grain interface (e.g. Bussian, 1983; Revil & Glover, 1998; Waxman & Smits, 1968). A wide  
 268 variety of formulations have been developed to account for both surface and bulk conduction. The  
 269 earlier models described the effect of surface conduction in terms of the volume of shale, while  
 270 more recent models attempt to account for the physics of the diffuse ion double layer surrounding  
 271 clay particles (e.g., Simandoux, 1963; Waxman and Smits, 1968; Clavier et al., 1984; Revil et al.,  
 272 1998). We choose to use the Waxman-Smits formula for partial brine saturation (Waxman &  
 273 Smits, 1968).

$$S_w = \left( \frac{\Phi^{-m} \rho_w}{\rho_t (1 + \rho_w B Q_v / S_w)} \right)^{\frac{1}{n}}, \quad (17)$$

$$B = 4.6 \left( 1 - 0.6 e^{-\frac{1}{1.3 \rho_w}} \right), \quad (18)$$

$$Q_v = \frac{\text{CEC}(1 - \Phi) D_o}{\Phi}, \quad (19)$$

274  
 275 where  $S_w$  is brine saturation,  $\rho_t$  is the measured sample resistivity,  $\rho_w$  is brine resistivity and  $\Phi$   
 276 is porosity.  $Q_v$  is the concentration of clay exchange cations or counter ions per unit pore volume  
 277 of the rock, and should be measured ideally in the laboratory by analyzing several samples with  
 278 different brine saturations (Waxman & Smits, 1968).  $B$  represents the average mobility of the

279 counter ions near the grain surfaces, CEC is the cation exchange capacity, and  $D_o$  is mineral  
280 grain density . The empirical parameters  $m$  and  $n$  are the cementation coefficient and the  
281 saturation exponent, respectively.

282 Zhan et al., (2010) showed experimentally for a similar porosity Berea sandstone (22.98 -  
283 23.60%) that the Waxman-Smits model gives reliable results for our salinity (Figure 6 of Zhan et  
284 al., 2010). Glover et al. (1994) presented laboratory data on the variation of Berea sandstone  
285 conductivity with fluid conductivity. They showed that, for low pore fluid conductivity ( $< 0.001$   
286 S/m), bulk conductivity is independent of pore fluid conductivity, and tends to be constant. For  
287 higher pore fluid conductivity ( $< 1$  S/m), the saturated rock conductivity is controlled mainly by  
288 the movement of ions through the bulk fluid, and seems to be independent of any surface  
289 conduction effect. As we used brine of 35 g/l (measured conductivity at 25 °C temperature is 5.2  
290 S/m), we are in the higher pore fluid conductivity zone where surface conduction effects have  
291 only a small effect on bulk rock conductivity. The experiments of Glover et al. (1994) and Zhan  
292 et al. (2010) had no hydrate, but hydrate is resistive compared to saline pore fluid and has  
293 negligible surface conduction (e.g., Lee & Collett, 2006a; Spangenberg, 2001). Several studies  
294 have shown that surface conduction contributes substantially to the macroscopic conductivity at  
295 low salinity and/or high temperature, even in low clay content sandstone (Bussian, 1983; Revil &  
296 Glover, 1998; Waxman & Smits, 1968). Since our sample has a low clay content of 2.3% by  
297 weight (XRD analysis; Han et al., 2015), the pore fluid has a high salinity (35gm/l NaCl with

298 conductivity of 5.22 S/m at 25 °C), and the temperature is low (5 °C), we conclude that the  
299 Waxman-Smits model should be applicable in our case.

300

301 As natural hydrate can be found also in clay rich sediments, appropriate clay conduction  
302 models should be used in such studies. We used the Waxman-Smits model but several  
303 modifications, refinements, or other models exist. For example, Clavier et al. (1984) proposed  
304 the dual water model, a modified form of the Waxman-Smits model with two types of pore  
305 water, of which only one is affected by surface conduction. Kan and Sen (1987) modelled clays  
306 as periodic arrays of charged insulating cylinders or spheres, immersed in symmetrical  
307 monovalent electrolyte. Revil and Glover (1998) discussed the theoretical framework of surface  
308 conduction predictions. Revil et al. (1998) accounted for the difference in behavior of anions and  
309 cations. de Lima & Sharma (1990) discussed a model based on shape and occurrence of clay,  
310 such as clay coating the sand grains or as individual clay grains. For a more detail review on  
311 conductivity models refer to, for example, Doveton (2001); Glover (2010); de Lima & Sharma  
312 (1990); Mavko et al. (1998).

313

314 The resistivity of brine is temperature-dependent and we calibrated it using the following  
315 expression (e.g., McCleskey et al., 2012):

$$\rho_w = \frac{\rho_{25}}{1+\alpha(T-25)}, \quad (20)$$

316 where,  $T$  (°C) is temperature,  $\alpha$  is the temperature compensation factor, and  $\rho_{25}$  ( $\Omega\text{m}$ ) is the  
317 resistivity of brine at 25 °C. Values of  $\rho_{25}$  were measured using a conductivity meter with  $\alpha =$

318 1.9%, similar to other studies (e.g. McCleskey et al., 2012). For a mixture of sand and clay, the  
319 CEC can be calculated from

$$CEC = m_c \sum \chi_i CEC_i, \quad (21)$$

320

321 where,  $m_c$  is the mass fraction of clay minerals in the whole rock,  $\chi_i$  is the relative volume fraction  
322 of each clay mineral, and  $CEC_i$  is the cation exchange capacity of each clay mineral. The cation  
323 exchange capacity of quartz can be neglected due to its large size (hence small amount of surface  
324 change per unit mass) in comparison to clay minerals (D. V. Ellis & Singer, 2007).

325

326 This method of calculating CEC assumes a mixture of sand and clay, and does not account  
327 for the various clay morphologies (e.g., clay as cement or grains) in Berea sandstone. We used  
328 0.09 meq/g CEC for authigenic illite (Thomas, 1976). A value of 2 was used for  $n$  (Waxman &  
329 Smits, 1968). The value of  $m$  was determined by fitting the initial resistivity for the known initial  
330 brine saturation, found to be 2.825, which is within the range of 1.3 to 4 reported by Jackson et al.,  
331 (1978). As hydrate forms, the value of  $m$  increases (Chen et al., 2008; Spangenberg, 2001), but  
332 the exact form of this increase is not known. To account for this change, we arbitrarily assumed a  
333 slightly higher value of  $m = 3.1$  for hydrate saturations above 5% (Chen et al., 2008; Spangenberg,  
334 2001). Spangenberg (2001) modelled the variation of  $n$  with water saturation, during hydrate  
335 formation. He showed,  $n$  increases significantly only for water saturation below 40% and  $n$  is

336 almost constant for water saturation above 40%. In our experiment water saturation started from  
337 83.5% and decreased up to 62% with hydrate formation; hence, we did not vary the value of  $n$ .

338

## 339 **4 RESULTS AND DISCUSSION**

340

### 341 **4.1 Three phase co-existence**

342 The results of the PT method provide evidence for the co-existence of methane gas,  
343 methane hydrate and brine in our experiments. When the pressure and temperature reached  
344 stability conditions, methane hydrate nucleation and growth started, followed by an increase in  
345 hydrate saturation and a decrease in gas and brine saturation (Figure 3). Even though we allowed  
346 enough time (80 - 180 h) for hydrate formation to continue (see Section 2 for further details), and  
347 there was always stoichiometrically sufficient methane gas and brine available for more methane  
348 hydrate formation, the reaction stabilized at a maximum methane hydrate saturation between 23-  
349 26% and methane gas saturation between 12-13% of the pore space (Figure 3). The maximum  
350 relative error in saturation calculated using the PT method is less than 0.5%. This phenomenon  
351 was observed also in two additional cycles of methane hydrate formation and dissociation,  
352 indicating the co-existence of three phases (gas, brine and hydrate) with similar maximum  
353 methane hydrate and methane gas saturations, and an asymptotic behavior of the saturation  
354 curves during hydrate formation in each cycle (Figure 3). At the maximum hydrate saturation,  
355 application of small perturbations in the confining pressure could have ruptured hydrate shells,  
356 trapping gas and allowed further hydrate formation (Fu et al., 2017). Such perturbations were not  
357 applied, so our estimate of co-existing gas may represent an upper bound for our experimental  
358 set up.

359 Methane hydrate is a non-stoichiometric solid with variable cage occupancy (Sloan &  
360 Koh, 2007). We used a hydration number of 6.39, corresponding to 90% cage occupancy (Sloan  
361 & Koh, 2007) for the calculation shown in Figure 3. If the cage occupancy is 100%,  $c$  is 5.75  
362 (Sloan & Koh, 2007) and the resulting maximum hydrate saturation decreases by 2 %.

363 In Section 1, we listed several mechanisms allowing three phase coexistence of methane  
364 gas with hydrate. Here, we discuss some of the mechanisms that are relevant to our experimental  
365 study. Methane hydrate may form when methane gas and water are in contact and have  
366 conditions favorable for hydrate formation. Our experimental pressure and temperature  
367 conditions of 8.8 MPa and 5 °C were well within the hydrate stability field for 35 g/L brine, but  
368 the salinity of the remaining pore water increases due to hydrate formation. Our experiments  
369 started with 35 g/L salinity, and a 26% hydrate saturation would have increased the mean salinity  
370 to about 46 g/L. At this salinity, our experimental pressure and temperature conditions are still  
371 within the GHSC (Figure 2a), as calculated using the approach of Tohidi et al., (1995). This  
372 calculation does not consider the effect of porous medium properties such as pore size, surface  
373 structure and mineral composition that can all affect the GHSC (e.g. Handa and Stupin, 1992;  
374 Clennell et al., 1999; Henry et al., 1999). Some experimental results suggest that surface  
375 structure and mineral composition may have little effect on GHSC (Riestenberg et al., 2003),  
376 while capillary effects due to pore size can be important (Clennell et al., 1999; Uchida et al.,  
377 2004). Therefore, we consider only capillary effects.

378  
379 Clennell et al., (1999) argued that methane hydrate behavior can be analogous to that of  
380 ice, as also suggested by other authors (e.g. Handa and Stupin, 1992). The freezing point of ice is  
381 lower in a fine-grained porous medium, such as soil, than in bigger pores, such as in sand. This is

382 due to curved water-ice interfaces that increase the free energy of pore water (Everett, 1961). In  
 383 small pores, the curvature is high and the excess free energy is also high. In big pores, the  
 384 curvature is low, and so is the excess free energy. Clennell et al. (1999) calculated the decrease  
 385 in the freezing point of ice inside a pore relative to the bulk freezing point (in a pore of infinite  
 386 pore radius), and extrapolated that to methane hydrate. We rearranged equation 8 of Clennell et  
 387 al. (1999) to calculate the minimum pore radius for which hydrate can form under our  
 388 experimental conditions of 8.8 MPa and 5 °C.

$$r_e = \frac{2\gamma_{iw}T_{i,bulk} \cos \theta_{iw}}{\rho_w \Delta H_{f,i} \Delta T_{i,pore}}, \quad (22)$$

389 where,  $r_e$  is the radius of the pores,  $\gamma_{iw}$  is the specific surface energy between ice and water,  
 390  $T_{i,bulk}$  is the absolute melting temperature of ice (without considering pore radius effects),  $\theta_{iw}$  is  
 391 the wetting angle,  $\rho_w$  is the density of water,  $\Delta H_{f,i}$  is the specific enthalpy of formation of ice  
 392 and  $\Delta T_{i,pore}$  is the change in melting temperature due to pore size effects. For our experimental  
 393 pressure of 8.8 MPa, the hydrate-water phase boundary temperature ( $T_{i,bulk}$ ) is 9.8 °C (calculated  
 394 using the approach of Tohidi et al., 1995), and therefore  $\Delta T_{i,pore}$  is -4.8 °C , giving a minimum  
 395 pore radius of 9.5 nm for  $\gamma_{iw} = 26.7 \text{ mJ m}^{-2}$  ,  $\theta_{iw} = 180$  degrees,  $\rho_w = 1000 \text{ kgm}^{-3}$  ,  $\Delta H_{f,i} = 333$   
 396  $\text{kJ Kg}^{-1}$  (Clennell et al., 1999).

397  
 398 We also measured the pore size distribution using X-ray computed tomography at the Swiss  
 399 Light Source (SLS) at the Paul Scherrer Institute. The optical objective used for imaging was  
 400 20x, which provided 325 nm voxel resolution. The pore size varied from 11.39  $\mu\text{m}$  to 73.11  $\mu\text{m}$ ,  
 401 so capillary effects in our sample should not have limited the formation of hydrate. Note that  
 402 only a small part (7.27 mm diameter and 8 mm high) of the sample was studied in the CT scan,

403 and we assumed that the observed pore size distribution is representative of the whole sample.  
404 Clennell et al.'s (1999) equation is for pure water, while our pore fluid had an average salinity of  
405 up to 46 g/L at maximum hydrate saturation. Sun and Duan (2007) developed a thermodynamic  
406 model for the effect of pore size and salinity on hydrate stability. We used their open online  
407 calculator ([models.kl-edu.cn/models.htm](http://models.kl-edu.cn/models.htm)) and found a minimum pore radius of less than 3.2  
408 nm, confirming the minor effect of pore size for our experimental conditions. We note also that it  
409 is very unlikely that hydrate formation can reduce the effective pore size to values close to the  
410 minimum pore radius because that could only happen when the pore is almost completely  
411 occupied by hydrate.

412

413         When hydrate forms, it can create a physical barrier between methane gas and water that  
414 prevents further hydrate formation. This physical barrier can be of various types:

415         a) Hydrate may form and dissociate only near the inlet pipe if the methane gas/brine is  
416 not distributed in the sample. This scenario is highly unlikely because the sample was vacuumed  
417 and then 83% of the pore space was filled with brine. These conditions were kept for three days,  
418 allowing the brine to spread within the sample. The gas would also be distributed within the  
419 sample before hydrate forms because: (i) the inlet pipe is on the lower surface of the sample, and  
420 methane gas would likely move upwards due to buoyancy; and (ii) methane gas was injected into  
421 the sample at room temperature and left for three days to complete its upward migration before  
422 cooling the system into the hydrate stability field.

423         b) Isolated pockets of gas or brine could exist in some pores. This can be due to gas  
424 reaching a pore that is not connected in the flow direction, and/or capillary trapping. If such a  
425 pore is blocked in the flow direction, hydrate formation can trap the gas (Figure 4, A). Similarly,

426 hydrate formation in connected pores could also disconnect them, trapping brine/gas (Figure 4,  
427 B). Capillary trapping can occur when the gas pressure is less than the capillary entry pressure of  
428 a given pore, which depends on its radius, resulting in the fluid being unable to move through  
429 that pore (Figure 4, C). The formation of hydrate can enhance this trapping mechanism by  
430 decreasing the effective pore radius, resulting in higher threshold capillary pressures needed for  
431 gas invasion (Figure 4, D).

432         c) Unconnected pores (occlusions) of gas/water can occur within hydrates (Figure 4, E).  
433 In our experiment, the maximum hydrate and gas saturations are around 26% and 12% of the  
434 pore space, respectively. Near seafloor sediments on the southern summit of Hydrate Ridge  
435 (offshore Oregon, USA) contain porous hydrates that likely formed when methane gas bubbles  
436 became coated with a hydrate film as they moved upwards within the sediments and coalesced  
437 together (Suess et al., 2001). A sufficiently thick hydrate film enveloping the methane bubbles  
438 disconnects the gas remaining inside the hydrate film from the pore water outside (Figure 4, F).  
439 Hence, gas remains trapped within the hydrate film, even though hydrate stability conditions  
440 prevail. Such porous hydrates have  $55 \pm 5$  % of their bulk volume filled with gas (Suess et al.,  
441 2001). Similar porous hydrate has also been recovered offshore Nigeria, with pore diameter of 2-  
442 3 mm (Sultan et al., 2014). We propose that this is the dominant mechanism for co-existing gas  
443 in our experimental setup. This mechanism does not involve three phase thermodynamic  
444 equilibrium, as the trapped methane gas inside the hydrate shell is not in physical contact with  
445 water outside the shell.

446         During drilling in a pockmark offshore Nigeria, Sultan et al. (2014) observed a vigorous  
447 flow of gas in the GHSZ, just after penetrating a thin hydrate layer at around 18 meters below  
448 sea floor. These authors attributed this flow to rapid influx of gas along fractures in the GHSZ,

449 which leads to rapid hydrate formation, primarily along the inner surface of fractures, leading to  
450 isolation of free gas from the surrounding pore fluid. This mechanism is similar to the one that  
451 we propose, but at much larger scale.

452 Gas trapped within hydrate films would diffuse out over geological time scales, so our  
453 experimental results might not reproduce well hydrate formation in nature. However, in a  
454 dynamic natural system with ongoing gas flow into the GHSZ, methane bubbles with a hydrate  
455 film enveloping them can also be present. Samples collected from the shallower sediments at  
456 Hydrate Ridge show that the residence time of such hydrate enveloped-methane bubbles may be  
457 less than the time needed for diffusion (Suess et al., 2001).

458 Further evidence for such gas trapping comes from a laboratory study of methane  
459 production by hydrate dissociation by heating that showed an abrupt peak in methane production  
460 rate, while the rate of water production remained almost constant (Tang et al., 2005), perhaps  
461 due to release of co-existing methane gas. A similar abrupt peak in methane production has been  
462 observed also using depressurization (Xiong et al., 2012).

463

#### 464 **4.2 Effect of co-existing gas within the GHSZ on hydrate saturation estimates**

465 Resistivity based methods for determining hydrate saturation do not differentiate between  
466 gas and hydrate; all resistive material in the pore space within the GHSZ is generally interpreted  
467 as hydrate (e.g., Hsu et al., 2014; Schwalenberg et al., 2010; Weitemeyer et al., 2006). Similarly,  
468 in our experiment, if we interpret all resistive material in the pore space as hydrate, the ERT  
469 method over-estimates the hydrate saturation because both gas and hydrate are resistive  
470 compared to brine (Figure 5). Small apparent fluctuations in the total amount of resistive  
471 material inferred from ERT results come from uncertainty when selecting the empirical

472 parameters in equation 17 (Section 3.2). The PT method can differentiate between methane gas  
473 and hydrate because gas and hydrate have different volumetric densities (Section 3.1). In our  
474 laboratory experiment, up to 36% of the resistive material remained as gas. In a borehole  
475 offshore Japan, the difference between hydrate saturation from resistivity methods and from  
476 sonic methods was *c.* 50%, likely due to co-existing gas (Miyakawa et al., 2014). Table 1 lists  
477 other field studies with differences in hydrate saturation inferred from resistivity methods and  
478 seismic/sonic methods.

479 Further uncertainties in methane quantification based on resistivity data can occur due to  
480 such co-existing gas. The methane content per unit volume of the gas phase is different to that of  
481 the hydrate phase. The difference depends on the molar volumes of hydrate and gas, which in  
482 turn depend on pressure and temperature, with greater variations in the gas phase than in the  
483 hydrate phase. Hence, the uncertainty in the methane inventory is larger in shallower water  
484 depths where gas molar volumes are higher. The methane content of the GHSZ is over-estimated  
485 in shallower waters (e.g., less than *c.* 1250 m depth for the Arctic Ocean) and under-estimated in  
486 deeper waters, where the molar volume of methane gas is less than that of hydrate. If the amount  
487 of co-existing gas within the GHSZ is significant, then it can affect the estimate of carbon  
488 content, and the geophysical and mechanical properties of the hydrate bearing sediments. Current  
489 numerical models that simulate the behavior of natural and laboratory hydrate systems do not  
490 account for this type of co-existing gas. Additional work is needed to support further our results,  
491 such as performing a similar study on different types of samples, and/or synchrotron X-ray  
492 computed tomography of hydrate- and gas-bearing samples.

493

## 494 **5 CONCLUSIONS**

495           In repeated cycles of hydrate formation and dissociation, our experimental results  
496 demonstrate the co-existence of up to 26% hydrate with about 12% gas. We infer that not all of  
497 the methane gas and water formed hydrate even when the two phase water-hydrate stability  
498 conditions were satisfied. We suggest such co-existence occurs when methane gas bubbles  
499 become enveloped in hydrate films. A sufficiently thick hydrate film would isolate the gas  
500 trapped inside from the brine outside, even when hydrate stability conditions prevail. Such  
501 methane bubbles enveloped in hydrate films have also been observed in samples from Hydrate  
502 Ridge, offshore Oregon USA, with up to 55% of the bulk hydrate volume made up of co-existing  
503 gas. Our experimental results show that hydrate formation from methane in the gas phase results  
504 in up to 36% co-existing gas (as a percentage of the bulk hydrate volume).

505           Our results support the idea that co-existing gas may be present within the gas hydrate  
506 stability zone in natural gas hydrate systems, with gas influx through fractures in fine-grained  
507 sediments. We suggest that this co-existence of gas and hydrate is one possible explanation for  
508 the differences in hydrate saturation estimates between resistivity and seismic/sonic observations  
509 of natural hydrate systems.

510 **ACKNOWLEDGMENTS**

511           We acknowledge funding from the UK Natural Environment Research Council (grant no  
512 NE/J020753/1). The data is available in the supplemental information and at the National  
513 Geoscience Data Centre, UK ([www.bgs.ac.uk/services/NGDC/home.html](http://www.bgs.ac.uk/services/NGDC/home.html)). Hydrate phase  
514 boundaries were calculated by the Centre for Gas Hydrate Research at Heriot-Watt University  
515 (<http://www.pet.hw.ac.uk/research/hydrate>), using the Heriot-Watt Hydrate and Phase  
516 Behaviour Programme (HWHYD). We thank K. Amalokwu and E. Attias for their advice on  
517 experimental troubleshooting. We thank P. J. Talling for his valuable comments on the  
518 manuscript. T. A. Minshull was supported by a Royal Society Wolfson Research Merit award.  
519 We also thank the editor Andre Revil, associate editor Ludmila Adam, reviewer Ingo Pecher and  
520 two other anonymous reviewers for their valuable comments.

521

522

523 **REFERENCE LIST**

- 524 Archie, G. E. (1942). The Electrical Resistivity Log as an Aid in Determining Some Reservoir  
525 Characteristics. *Transactions of the AIME*, 146(1), 54–62. <https://doi.org/10.2118/942054-G>
- 526 Attias, E., Weitemeyer, K. A., Minshull, T. A., Best, A. I., Sinha, M., Jegen-Kulcsar, M., ...  
527 Berndt, C. (2016). Controlled-source electromagnetic and seismic delineation of subseafloor  
528 fluid flow structures in a gas hydrate province, offshore Norway. *Geophysical Journal*  
529 *International*, 206(2), 1093–1110. <https://doi.org/10.1093/gji/ggw188>
- 530 Bussian, A. E. (1983). Electrical conductance in a porous medium. *Geophysics*, 48(9), 1258–  
531 1268. <https://doi.org/10.1190/1.1441549>
- 532 Chaouachi, M., Falenty, A., Sell, K., Enzmann, F., Kersten, M., Haberthür, D., & Kuhs, W. F.  
533 (2015). Microstructural evolution of gas hydrates in sedimentary matrices observed with  
534 synchrotron X-ray computed tomographic microscopy. *Geochemistry, Geophysics,*  
535 *Geosystems*, 16(6), 1711–1722. <https://doi.org/10.1002/2015GC005811>
- 536 Chen, M. P., Riedel, M., Spence, G. D., & Hyndman, R. D. (2008). Data report: a downhole  
537 electrical resistivity study of northern Cascadia marine gas hydrate. *Proceedings of the*  
538 *Integrated Drilling Program*, 311. <https://doi.org/10.2204/iodp.proc.311.203.2008>
- 539 Clavier, C., Coates, G., & Dumanoir, J. (1984). Theoretical and Experimental Bases for the  
540 Dual-Water Model for Interpretation of Shaly Sands. *Society of Petroleum Engineers*  
541 *Journal*, 24(2), 153–168. <https://doi.org/10.2118/6859-PA>
- 542 Clennell, M. Ben, Hovland, M., Booth, J. S., Henry, P., & Winters, W. J. (1999). Formation of

543 natural gas hydrates in marine sediments: 1. Conceptual model of gas hydrate growth  
544 conditioned by host sediment properties. *Journal of Geophysical Research: Solid Earth*,  
545 *104*(B10), 22985–23003. <https://doi.org/10.1029/1999JB900175>

546 Doveton, J. H. (2001). All Models Are Wrong , but Some Models Are Useful : “ Solving ” the  
547 Simandoux Equation Prolog : The Archie Equation.

548 Ellis, D. V., & Singer, J. M. (2007). *Well Logging for Earth Scientists*. (D. V. Ellis & J. M.  
549 Singer, Eds.). Dordrecht: Springer Netherlands. <https://doi.org/10.1007/978-1-4020-4602-5>

550 Ellis, M. H. (2008). *Joint Seismic and Electrical Measurements of Gas Hydrates in Continental*  
551 *Margin Sediments*. PhD thesis, University of Southampton. Retrieved from  
552 <http://eprints.soton.ac.uk/id/eprint/63293>

553 Everett, D. H. (1961). The thermodynamics of frost damage to porous solids. *Transactions of the*  
554 *Faraday Society*, *57*(0), 1541. <https://doi.org/10.1039/tf9615701541>

555 Fohrmann, M., & Pecher, I. A. (2012). Analysing sand-dominated channel systems for potential  
556 gas-hydrate-reservoirs using an AVO seismic inversion technique on the Southern  
557 Hikurangi Margin, New Zealand. *Marine and Petroleum Geology*, *38*(1), 19–34.  
558 <https://doi.org/10.1016/j.marpetgeo.2012.08.001>

559 Fu, X., Porter, M., Viswanathan, H., Carey, J., & Juanes, R. (2017). Controlled depressurization  
560 of a hydrate-crust gas bubble : Insights from 2D experiments and phase-field modeling. In  
561 *The 9th International Conference on Gas Hydrates*. Denver. Retrieved from  
562 [http://icgh9.csm.space.com/docs/ICGH9\\_FinalProgram.pdf?062017](http://icgh9.csm.space.com/docs/ICGH9_FinalProgram.pdf?062017)

563 Fujii, T., Suzuki, K., Takayama, T., Tamaki, M., Komatsu, Y., Konno, Y., ... Nagao, J. (2015).  
564 Geological setting and characterization of a methane hydrate reservoir distributed at the first  
565 offshore production test site on the Daini-Atsumi Knoll in the eastern Nankai Trough,  
566 Japan. *Marine and Petroleum Geology*, 66, 310–322.  
567 <https://doi.org/10.1016/j.marpetgeo.2015.02.037>

568 Glover, P. W. J. (2010). A generalized Archie's law for n phases. *GEOPHYSICS*, 75(6), E247–  
569 E265. <https://doi.org/10.1190/1.3509781>

570 Glover, P. W. J., Meredith, P. G., Sammonds, P. R., & Murrell, S. A. F. (1994). Ionic surface  
571 electrical conductivity in sandstone. *Journal of Geophysical Research: Solid Earth*,  
572 99(B11), 21635–21650. <https://doi.org/10.1029/94JB01474>

573 Gorman, A. R., Holbrook, W. S., Hornbach, M. J., Hackwith, K. L., Lizarralde, D., & Pecher, I.  
574 (2002). Migration of methane gas through the hydrate stability zone in a low-flux hydrate  
575 province. *Geology*, 30(4), 327. [https://doi.org/10.1130/0091-  
576 7613\(2002\)030<0327:MOMGTT>2.0.CO;2](https://doi.org/10.1130/0091-7613(2002)030<0327:MOMGTT>2.0.CO;2)

577 Goswami, B. K., Weitemeyer, K. A., Minshull, T. A., Sinha, M. C., Westbrook, G. K., Chabert,  
578 A., ... Ker, S. (2015). A joint electromagnetic and seismic study of an active pockmark  
579 within the hydrate stability field at the Vestnesa Ridge, West Svalbard margin. *Journal of*  
580 *Geophysical Research: Solid Earth*, 120(10), 6797–6822.  
581 <https://doi.org/10.1002/2015JB012344>

582 Guerin, G., Goldberg, D., & Meltser, A. (1999). Characterization of in situ elastic properties of  
583 gas hydrate-bearing sediments on the Blake Ridge. *Journal of Geophysical Research: Solid*

584 *Earth*, 104(B8), 17781–17795. <https://doi.org/10.1029/1999JB900127>

585 Han, T., Best, A. I., Sothcott, J., & Macgregor, L. M. (2011). Pressure effects on the joint elastic-  
586 electrical properties of reservoir sandstones. *Geophysical Prospecting*, 59(3), 506–517.  
587 <https://doi.org/10.1111/j.1365-2478.2010.00939.x>

588 Han, T., Best, A. I., Sothcott, J., North, L. J., & MacGregor, L. M. (2015). Relationships among  
589 low frequency (2Hz) electrical resistivity, porosity, clay content and permeability in  
590 reservoir sandstones. *Journal of Applied Geophysics*, 112, 279–289.  
591 <https://doi.org/10.1016/j.jappgeo.2014.12.006>

592 Handa, Y. P., & Stupin, D. (1992). Thermodynamic properties and dissociation characteristics of  
593 methane and propane hydrates in 70-angstrom-radius silica-gel pores. *Journal of Physical  
594 Chemistry*, 96(21), 8599–8603. <https://doi.org/10.1021/j100200a071>

595 Henry, P., Thomas, M., & Clennell, M. Ben. (1999). Formation of natural gas hydrates in marine  
596 sediments: 2. Thermodynamic calculations of stability conditions in porous sediments.  
597 *Journal of Geophysical Research: Solid Earth*, 104(B10), 23005–23022.  
598 <https://doi.org/10.1029/1999JB900167>

599 Hesse, R., & Harrison, W. E. (1981). Gas hydrates (clathrates) causing pore-water freshening  
600 and oxygen isotope fractionation in deep-water sedimentary sections of terrigenous  
601 continental margins. *Earth and Planetary Science Letters*, 55(3), 453–462.  
602 [https://doi.org/10.1016/0012-821X\(81\)90172-2](https://doi.org/10.1016/0012-821X(81)90172-2)

603 Hsu, S. K., Chiang, C. W., Evans, R. L., Chen, C. S., Chiu, S. D., Ma, Y. F., ... Wang, Y.  
604 (2014). Marine controlled source electromagnetic method used for the gas hydrate

605 investigation in the offshore area of SW Taiwan. *Journal of Asian Earth Sciences*, 92, 224–  
606 232. <https://doi.org/10.1016/j.jseaes.2013.12.001>

607 Hustoft, S., Bünz, S., Mienert, J., & Chand, S. (2009). Gas hydrate reservoir and active methane-  
608 venting province in sediments on <20 Ma young oceanic crust in the Fram Strait, offshore  
609 NW-Svalbard. *Earth and Planetary Science Letters*, 284(1–2), 12–24.  
610 <https://doi.org/10.1016/j.epsl.2009.03.038>

611 Hwang, M. J., Wright, D. A., Kapur, A., & Holder, G. D. (1990). An experimental study of  
612 crystallization and crystal growth of methane hydrates from melting ice. *Journal of*  
613 *Inclusion Phenomena and Molecular Recognition in Chemistry*, 8(1–2), 103–116.  
614 <https://doi.org/10.1007/BF01131291>

615 Jackson, P. D., Smith, D. T., & Stanford, P. N. (1978). Resistivity-porosity-particle shape  
616 relationships for marine sands. *Geophysics*, 43(6), 1250–1268.  
617 <https://doi.org/10.1190/1.1440891>

618 Kan, R., & Sen, P. N. (1987). Electrolytic conduction in periodic arrays of insulators with  
619 charges. *The Journal of Chemical Physics*, 86(10), 5748–5756.  
620 <https://doi.org/10.1063/1.452502>

621 Kvenvolden, K. A. (1993). Gas hydrates—geological perspective and global change. *Reviews of*  
622 *Geophysics*, 31(2), 173. <https://doi.org/10.1029/93RG00268>

623 Lee, M. W., & Collett, T. S. (2006a). A Method of Shaly Sand Correction for Estimating Gas  
624 Hydrate Saturations Using Downhole Electrical Resistivity Log Data. *U.S. Geological*  
625 *Survey Scientific Investigations Report*, 1–10. Retrieved from

626 [https://pubs.usgs.gov/sir/2006/5121/pdf/sir5121\\_508.pdf](https://pubs.usgs.gov/sir/2006/5121/pdf/sir5121_508.pdf)

627 Lee, M. W., & Collett, T. S. (2006b). Gas Hydrate and Free Gas Saturations Estimated from  
628 Velocity Logs on Hydrate Ridge, offshore Oregon, U.S.A. In *Proceedings of the Ocean*  
629 *Drilling Program, 199 Scientific Results* (Vol. 204, pp. 1–25). Ocean Drilling Program.  
630 <https://doi.org/10.2973/odp.proc.sr.204.103.2006>

631 Lee, M. W., & Collett, T. S. (2008). Integrated analysis of well logs and seismic data to estimate  
632 gas hydrate concentrations at Keathley Canyon, Gulf of Mexico. *Marine and Petroleum*  
633 *Geology*, 25(9), 924–931. <https://doi.org/10.1016/j.marpetgeo.2007.09.002>

634 de Lima, O. a. L., & Sharma, M. M. (1990). A grain conductivity approach to shaly sandstones.  
635 *GEOPHYSICS*, 55(10), 1347–1356. <https://doi.org/10.1190/1.1442782>

636 Liu, X., & Flemings, P. B. (2006). Passing gas through the hydrate stability zone at southern  
637 Hydrate Ridge, offshore Oregon. *Earth and Planetary Science Letters*, 241(1–2), 211–226.  
638 <https://doi.org/10.1016/j.epsl.2005.10.026>

639 Lu, Z., & Sultan, N. (2008). Empirical expressions for gas hydrate stability law, its volume  
640 fraction and mass-density at temperatures 273.15 K to 290.15 K. *Geochemical Journal*,  
641 42(2), 163–175. Retrieved from <http://archimer.ifremer.fr/doc/00000/4958/>

642 Mavko, G. M., Mukerji, T., & Dvorkin. (1998). The Rock Physics Handbook. Tools for Seismic  
643 Analysis in Porous Media. x + 329 pp. Cambridge, New York, Melbourne: Cambridge  
644 University Press. Price £40.00, US \$64.95 (hard covers). ISBN 0 521 62068 6. *Geological*  
645 *Magazine*, 136(6), 697–711. <https://doi.org/10.1017/S0016756899413329>

- 646 McCleskey, R. B., Nordstrom, D. K., & Ryan, J. N. (2012). Comparison of electrical  
647 conductivity calculation methods for natural waters. *Limnology and Oceanography:  
648 Methods*, 10(11), 952–967. <https://doi.org/10.4319/lom.2012.10.952>
- 649 Milkov, A. V., Dickens, G. R., Claypool, G. E., Lee, Y. J., Borowski, W. S., Torres, M. E., ...  
650 Schultheiss, P. (2004). Co-existence of gas hydrate, free gas, and brine within the regional  
651 gas hydrate stability zone at Hydrate Ridge (Oregon margin): Evidence from prolonged  
652 degassing of a pressurized core. *Earth and Planetary Science Letters*, 222(3–4), 829–843.  
653 <https://doi.org/10.1016/j.epsl.2004.03.028>
- 654 Millero, F. J., Chen, C.-T., Bradshaw, A., & Schleicher, K. (1980). A new high pressure equation  
655 of state for seawater. *Deep Sea Research Part A. Oceanographic Research Papers*, 27(3–4),  
656 255–264. [https://doi.org/10.1016/0198-0149\(80\)90016-3](https://doi.org/10.1016/0198-0149(80)90016-3)
- 657 Miyakawa, A., Saito, S., Yamada, Y., Tomaru, H., Kinoshita, M., & Tsuji, T. (2014). Gas  
658 hydrate saturation at Site C0002, IODP Expeditions 314 and 315, in the Kumano Basin,  
659 Nankai trough. *Island Arc*, 23(2), 142–156. <https://doi.org/10.1111/iar.12064>
- 660 North, L. J., Best, A. I., Sothcott, J., & MacGregor, L. (2013). Laboratory determination of the  
661 full electrical resistivity tensor of heterogeneous carbonate rocks at elevated pressures.  
662 *Geophysical Prospecting*, 61(2), 458–470. [https://doi.org/10.1111/j.1365-  
663 2478.2012.01113.x](https://doi.org/10.1111/j.1365-2478.2012.01113.x)
- 664 Peng, D.-Y., & Robinson, D. B. (1976). A New Two-Constant Equation of State. *Industrial &  
665 Engineering Chemistry Fundamentals*, 15(1), 59–64. <https://doi.org/10.1021/i160057a011>
- 666 Plaza-Faverola, A., Westbrook, G. K., Ker, S., Exley, R. J. K., Gailler, A., Minshull, T. A., &

667 Broto, K. (2010). Evidence from three-dimensional seismic tomography for a substantial  
668 accumulation of gas hydrate in a fluid-escape chimney in the Nyegga pockmark field,  
669 offshore Norway. *Journal of Geophysical Research: Solid Earth*, 115(8), 1–24.  
670 <https://doi.org/10.1029/2009JB007078>

671 Priest, J. A., Rees, E. V. L., & Clayton, C. R. I. (2009). Influence of gas hydrate morphology on  
672 the seismic velocities of sands. *Journal of Geophysical Research: Solid Earth*, 114(B11),  
673 B11205. <https://doi.org/10.1029/2009JB006284>

674 Revil, A., & Glover, P. W. J. (1998). Nature of surface electrical conductivity in natural sands,  
675 sandstones, and clays. *Geophysical Research Letters*, 25(5), 691–694.  
676 <https://doi.org/10.1029/98GL00296>

677 Revil, A., Cathles, L. M., Losh, S., & Nunn, J. a. (1998). Electrical conductivity in shaly sands  
678 with geophysical applications. *Journal of Geophysical Research*, 103, 23,925-23,936.  
679 <https://doi.org/10.1029/98JB02125>

680 Riestenberg, D., West, O., Lee, S., McCallum, S., & Phelps, T. J. (2003). Sediment surface  
681 effects on methane hydrate formation and dissociation. *Marine Geology*, 198(1–2), 181–  
682 190. [https://doi.org/10.1016/S0025-3227\(03\)00100-2](https://doi.org/10.1016/S0025-3227(03)00100-2)

683 Rutter, E. H., & Glover, C. T. (2012). The deformation of porous sandstones; are Byerlee friction  
684 and the critical state line equivalent? *Journal of Structural Geology*, 44, 129–140.  
685 <https://doi.org/10.1016/j.jsg.2012.08.014>

686 Schicks, J. M., Naumann, R., Erzinger, J., Hester, K. C., Koh, C. A., & Sloan, E. D. (2006).  
687 Phase transitions in mixed gas hydrates: Experimental observations versus calculated data.

688 *Journal of Physical Chemistry B*, 110(23), 11468–11474. <https://doi.org/10.1021/jp0612580>

689 Schnurle, P., Liu, C.-S., Hsuan, T.-H., & Wang, T.-K. (2004). Characteristics of Gas Hydrate  
690 and Free Gas Offshore Southwestern Taiwan from a Combined MCS/OBS Data Analysis.  
691 *Marine Geophysical Researches*, 25(1–2), 157–180. [https://doi.org/10.1007/s11001-005-](https://doi.org/10.1007/s11001-005-0740-6)  
692 0740-6

693 Schwalenberg, K., Haeckel, M., Poort, J., & Jegen, M. (2010). Evaluation of gas hydrate deposits  
694 in an active seep area using marine controlled source electromagnetics: Results from  
695 Opouawe Bank, Hikurangi Margin, New Zealand. *Marine Geology*, 272(1–4), 79–88.  
696 <https://doi.org/10.1016/j.margeo.2009.07.006>

697 Simandoux, P. (1963). Dielectric measurements in porous media and application to shaly  
698 formations. *Rev. Inst. Fr. Petrol.*, 18(Suppl. issue), 193–215.

699 Skinner, B. J. (1966). Thermal Expansion. In J. Clark Sydney P. (Ed.), *Handbook of Physical*  
700 *Constants* (pp. 75–96). Geological Society of America. <https://doi.org/10.1130/MEM97-p75>

701 Sloan, E. D., & Koh, C. A. (2007). *Clathrate hydrates of natural gases*. New York: CRC Press.  
702 Retrieved from [https://www.crcpress.com/Clathrate-Hydrates-of-Natural-Gases-Third-](https://www.crcpress.com/Clathrate-Hydrates-of-Natural-Gases-Third-Edition/Sloan-Jr-Koh/p/book/9780849390784)  
703 [Edition/Sloan-Jr-Koh/p/book/9780849390784](https://www.crcpress.com/Clathrate-Hydrates-of-Natural-Gases-Third-Edition/Sloan-Jr-Koh/p/book/9780849390784)

704 Smith, A. J., Flemings, P. B., Liu, X., & Darnell, K. (2014). The evolution of methane vents that  
705 pierce the hydrate stability zone in the world’s oceans. *Journal of Geophysical Research B:*  
706 *Solid Earth*, 119(8), 6337–6356. <https://doi.org/10.1002/2013JB010686>

707 Spangenberg, E. (2001). Modeling of the influence of gas hydrate content on the electrical

708 properties of porous sediments. *Journal of Geophysical Research: Solid Earth*, 106(B4),  
709 6535–6548. <https://doi.org/10.1029/2000JB900434>

710 Suess, E., Torres, M. E., Bohrmann, G., Collier, R. W., Rickert, D., Goldfinger, C., ... Elver, M.  
711 (2001). Sea Floor Methane Hydrates at Hydrate Ridge, Cascadia Margin. In *Natural Gas*  
712 *Hydrates—Occurrence, Distribution and Detection* (pp. 87–98). American Geophysical  
713 Union. <https://doi.org/10.1029/GM124p0087>

714 Sultan, N., Bohrmann, G., Ruffine, L., Pape, T., Riboulot, V., Colliat, J. L., ... Wei, J. (2014).  
715 Journal of Geophysical Research : Solid Earth. *Journal of Geophysical Research: Solid*  
716 *Earth*, 119(December 2011), 2679–2694. <https://doi.org/10.1029/2010JB007453>. Pockmark

717 Sultaniya, A. K., Priest, J. A., & Clayton, C. R. I. (2015). Measurements of the changing wave  
718 velocities of sand during the formation and dissociation of disseminated methane hydrate.  
719 *Journal of Geophysical Research: Solid Earth*, 120(2), 778–789.  
720 <https://doi.org/10.1002/2014JB011386>

721 Sun, R., & Duan, Z. (2007). An accurate model to predict the thermodynamic stability of  
722 methane hydrate and methane solubility in marine environments. *Chemical Geology*,  
723 244(1–2), 248–262. <https://doi.org/10.1016/j.chemgeo.2007.06.021>

724 Tang, L. G., Xiao, R., Huang, C., Feng, Z. P., & Fan, S. S. (2005). Experimental investigation of  
725 production behavior of gas hydrate under thermal stimulation in unconsolidated sediment.  
726 *Energy and Fuels*, 19(6), 2402–2407. <https://doi.org/10.1021/ef050223g>

727 Thomas, E. C. (1976). The Determination of  $Q_v$  From Membrane Potential Measurements on  
728 Shaly Sands. *Journal of Petroleum Technology*, 28(9), 1087–1096.

729 <https://doi.org/10.2118/5505-PA>

730 Tishchenko, P., Hensen, C., Wallmann, K., & Wong, C. S. (2005). Calculation of the stability  
731 and solubility of methane hydrate in seawater. *Chemical Geology*, 219(1–4), 37–52.  
732 <https://doi.org/10.1016/j.chemgeo.2005.02.008>

733 Tohidi, B., Danesh, A., & Todd, A. C. (1995). Modelling single and mixed electrolyte solutions  
734 and its applications to gas hydrates. *Chemical Engineering Research and Design*, 73(A4),  
735 464–472. Retrieved from [http://www.scopus.com/inward/record.url?eid=2-s2.0-](http://www.scopus.com/inward/record.url?eid=2-s2.0-0029301853&partnerID=tZOtx3y1)  
736 [0029301853&partnerID=tZOtx3y1](http://www.scopus.com/inward/record.url?eid=2-s2.0-0029301853&partnerID=tZOtx3y1)

737 Torres, M. E., Wallmann, K., Tréhu, A. M., Bohrmann, G., Borowski, W. S., & Tomaru, H.  
738 (2004). Gas hydrate growth, methane transport, and chloride enrichment at the southern  
739 summit of Hydrate Ridge, Cascadia margin off Oregon. *Earth and Planetary Science*  
740 *Letters*, 226(1–2), 225–241. <https://doi.org/10.1016/j.epsl.2004.07.029>

741 Uchida, T., Takeya, S., Chuvilin, E. M., Ohmura, R., Nagao, J., Yakushev, V. S., ... Narita, H.  
742 (2004). Decomposition of methane hydrates in sand, sandstone, clays and glass beads.  
743 *Journal of Geophysical Research: Solid Earth*, 109(5), 1–12.  
744 <https://doi.org/10.1029/2003JB002771>

745 Vafaei, M. T., Kvamme, B., Chejara, A., & Jemai, K. (2014). A new reservoir simulator for  
746 studying hydrate dynamics in reservoir. *International Journal of Greenhouse Gas Control*,  
747 23, 12–21. <https://doi.org/10.1016/j.ijggc.2014.02.001>

748 Waite, W. F., Winters, W. J., & Mason, D. H. (2004). Methane hydrate formation in partially  
749 water-saturated Ottawa sand. *American Mineralogist*, 89(July), 1202–1207.

- 750 <https://doi.org/10.2138/am-2004-8-906>
- 751 Waxman, M. H., & Smits, L. J. M. (1968). Electrical Conductivities in Oil-Bearing Shaly Sands.  
752 *Society of Petroleum Engineers Journal*, 8(2), 107–122. <https://doi.org/10.2118/1863-A>
- 753 Weitemeyer, K. A., Constable, S. C., Key, K. W., & Behrens, J. P. (2006). First results from a  
754 marine controlled-source electromagnetic survey to detect gas hydrates offshore Oregon.  
755 *Geophysical Research Letters*, 33(3), 1–4. <https://doi.org/10.1029/2005GL024896>
- 756 White, R. S. (1977). Seismic bright spots in the Gulf of Oman. *Earth and Planetary Science*  
757 *Letters*, 37(1), 29–37. [https://doi.org/10.1016/0012-821X\(77\)90143-1](https://doi.org/10.1016/0012-821X(77)90143-1)
- 758 William J. Winters, Pecher, I. A., Waite, W. F., & David H. Mason. (2004). Physical Properties  
759 and Rock Physics Models of Sediment Containing Natural and Laboratory-formed Methane  
760 Gas Hydrate. *American Mineralogist*, 89, 1221–1227. [https://doi.org/10.2138/am-2004-8-](https://doi.org/10.2138/am-2004-8-909)  
761 909
- 762 Xiong, L., Li, X., Wang, Y., & Xu, C. (2012). Experimental study on methane hydrate  
763 dissociation by depressurization in porous sediments. *Energies*, 5(2), 518–530.  
764 <https://doi.org/10.3390/en5020518>
- 765 Yang, L., Falenty, A., Chaouachi, M., Haberthür, D., & Kuhs, W. F. (2016). Synchrotron X-ray  
766 computed microtomography study on gas hydrate decomposition in a sedimentary matrix.  
767 *Geochemistry, Geophysics, Geosystems*, 17(9), 3717–3732.  
768 <https://doi.org/10.1002/2016GC006521>
- 769 You, K., Kneafsey, T. J., Flemings, P. B., Polito, P., & Bryant, S. L. (2015). Salinity-buffered

770 methane hydrate formation and dissociation in gas-rich systems. *Journal of Geophysical*  
771 *Research: Solid Earth*, 120(2), 643–661. <https://doi.org/10.1002/2014JB011190>

772 Zhan, X., Schwartz, L. M., Toksöz, M. N., Smith, W. C., & Morgan, F. D. (2010). Pore-scale  
773 modeling of electrical and fluid transport in Berea sandstone. *Geophysics*, 75(5), F135–  
774 F142. <https://doi.org/10.1190/1.3463704>

775

776

777 **TABLE 1. HYDRATE SATURATIONS FROM RESISTIVITY AND SEISMIC/SONIC**  
 778 **METHODS**

Location	Hydrate Saturation (%)		References	Comments
	Resistivity	Seismic/ Sonic		
Good Weather Ridge, Taiwan	15-16	0-10	1, 2	Seismic: broad area
Hikurangi Margin, NZ	~34	~25	3, 4	Maximum
ODP Leg 204, USA			5	
	6.5 ± 3.9	10.2 ± 3.7		
Site 1244	7.9 ± 5.5	10.4 ± 5.6		
Site 1245	4.5 ± 2.8	6.1 ± 3.2		
Site 1247				
Kumano Basin, Japan	0-80	0-30	6	Parts of well
Nyegga, Norway	38	14-27	7, 8	In chimney
Vestnesa Ridge, Norway	20-30	~11	9, 10	Outside chimney

*Note:* <sup>1</sup> Schnurle et al., 2004; <sup>2</sup> Hsu et al., 2014; <sup>3</sup> Fohrmann and Pecher, 2012; <sup>4</sup> Schwalenberg et al., 2010; <sup>5</sup> Lee & Collett, 2006; <sup>6</sup> Miyakawa et al., 2014; <sup>7</sup> Attias et al., 2016; <sup>8</sup> Plaza-Faverola et al., 2010; <sup>9</sup> Goswami et al., 2015; <sup>10</sup> Hustoft et al., 2009.

779

780

**TABLE 2. PARAMETERS USED IN THE PT METHOD.**

781

Description	Symbol*
Number of moles of methane hydrate	$n_h$
Saturation of methane hydrate	$S_h$
Pore fluid Pressure	$p$
Total pore space in the sample	$V_{ts}$
Volume of methane gas in the sample	$V_{ms}$
Volume of liquid water in the sample	$V_w$
Volume of hydrate in the sample	$V_h$
Volume of pipe	$V_p$
Total number of moles of methane in the system	$n_t$
Number of moles of methane gas in pipe	$n_p$
Number of moles of methane gas in sample	$n_s$
Number of moles of methane in solution	$n_{sw}$
Number of moles of water in liquid phase	$n_w$
Temperature in the pipe	$T_p$
Temperature in the sample	$T_s$
Compressibility of methane gas in the pipe	$Z_p$
Compressibility of methane gas in the sample	$Z_s$
Density of Brine	$D_w$
Density of Hydrate	$D_h$

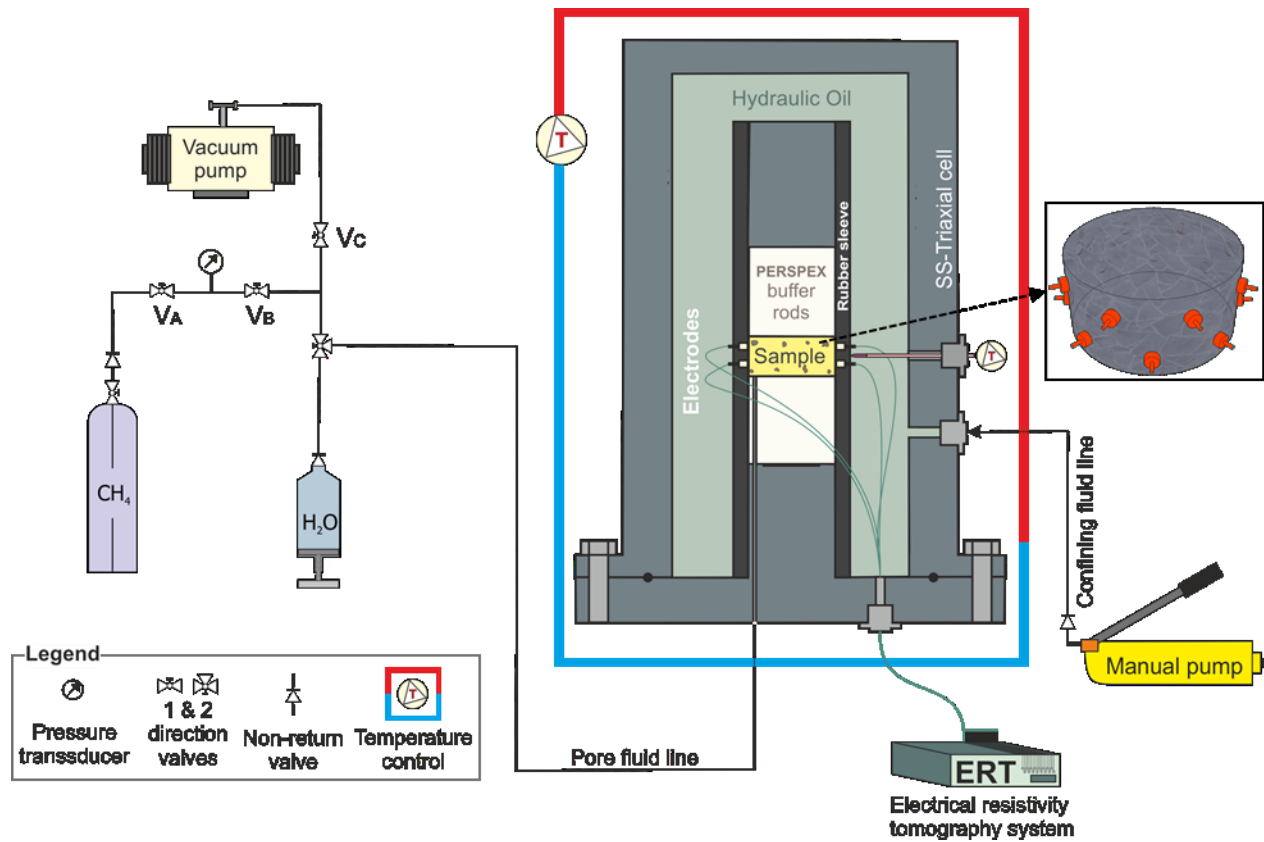
---

782 \*Initial values for these parameters are denoted in the text with a subscript 0

**TABLE 3. CONSTANTS USE IN THE PT METHOD.**

Description	Symbol	Values
Ratio of water to methane in hydrate (Sloan & Koh, 2007)	c	6.39
Molar mass of brine (35 g/L)	$M_w$	0.0186 Kg
Molar mass of hydrate (structure I)	$M_h$	0.1312 Kg
Universal gas constant	R	$8.314 \text{ Jmol}^{-1}\text{K}^{-1}$

785



786

787 Figure 1: Schematic diagram of the experimental setup, also showing the arrangement of

788 electrodes around the Berea rock sample (5 cm diameter). Scales are approximate.

789

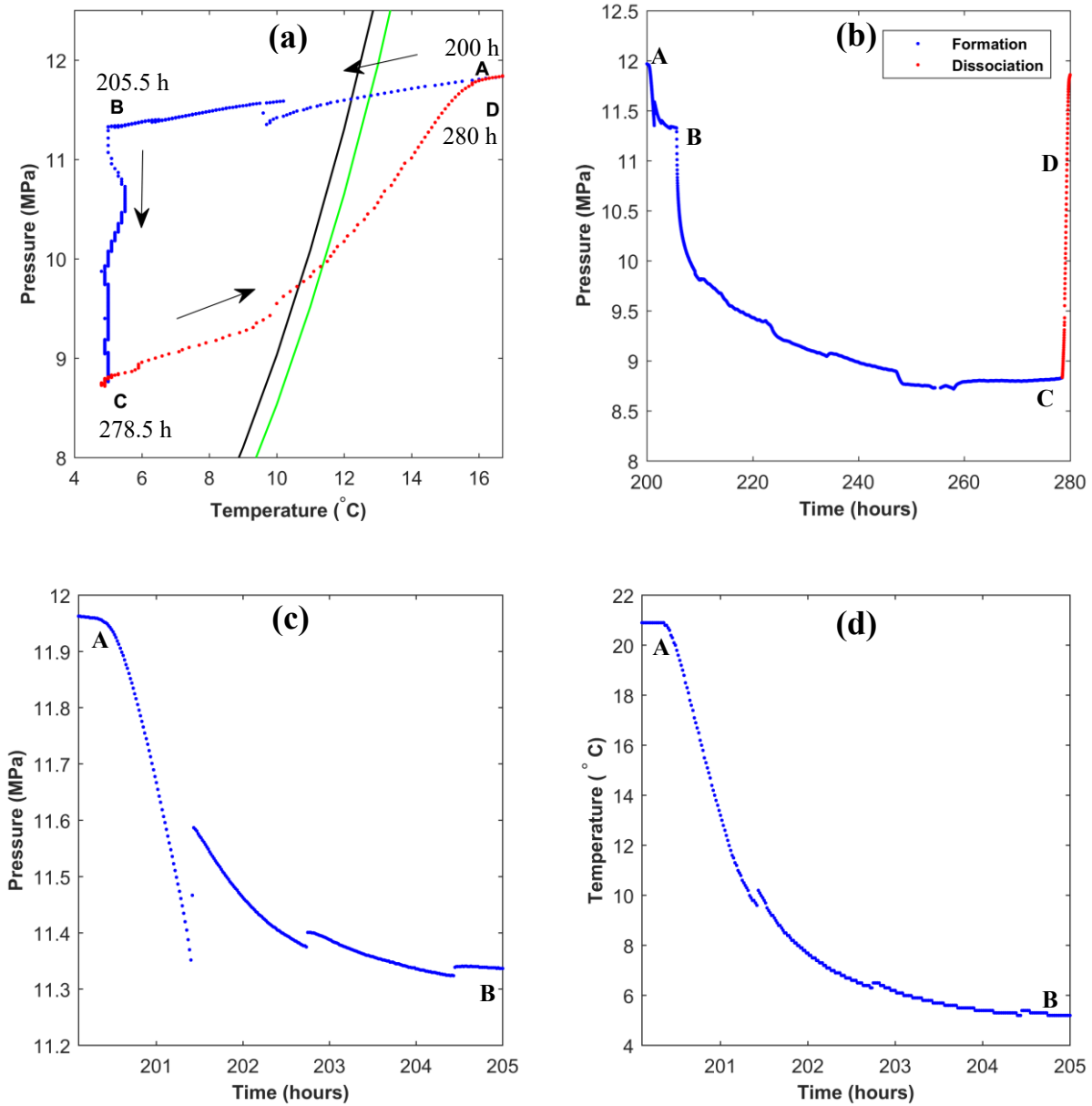
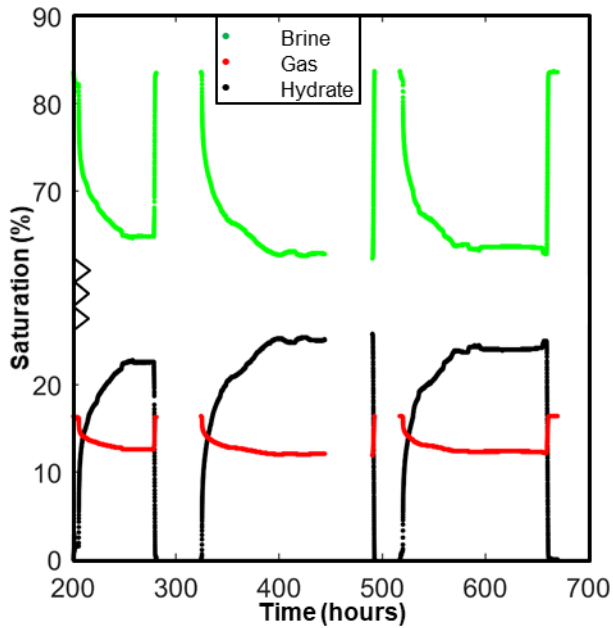


Figure 2. Changes of a) pressure versus temperature, and b) pressure with time during methane hydrate formation and dissociation in Berea sandstone. Only the second cycle of hydrate formation and dissociation is shown for clarity. The green and black lines are the pure methane hydrate phase boundary for 35 g/L and 46 g/L salinity respectively, calculated using the approach of Tohidi et al. (1995). Blue dots represent cooling and red dots represent heating. In

a) time is shown in hours (h). Trajectory ABC marks cooling of the system to 5 °C and hydrate formation. Trajectory CD shows hydrate dissociation. c) and d) show pressure and temperature change with time during trajectory AB. See text for further details.

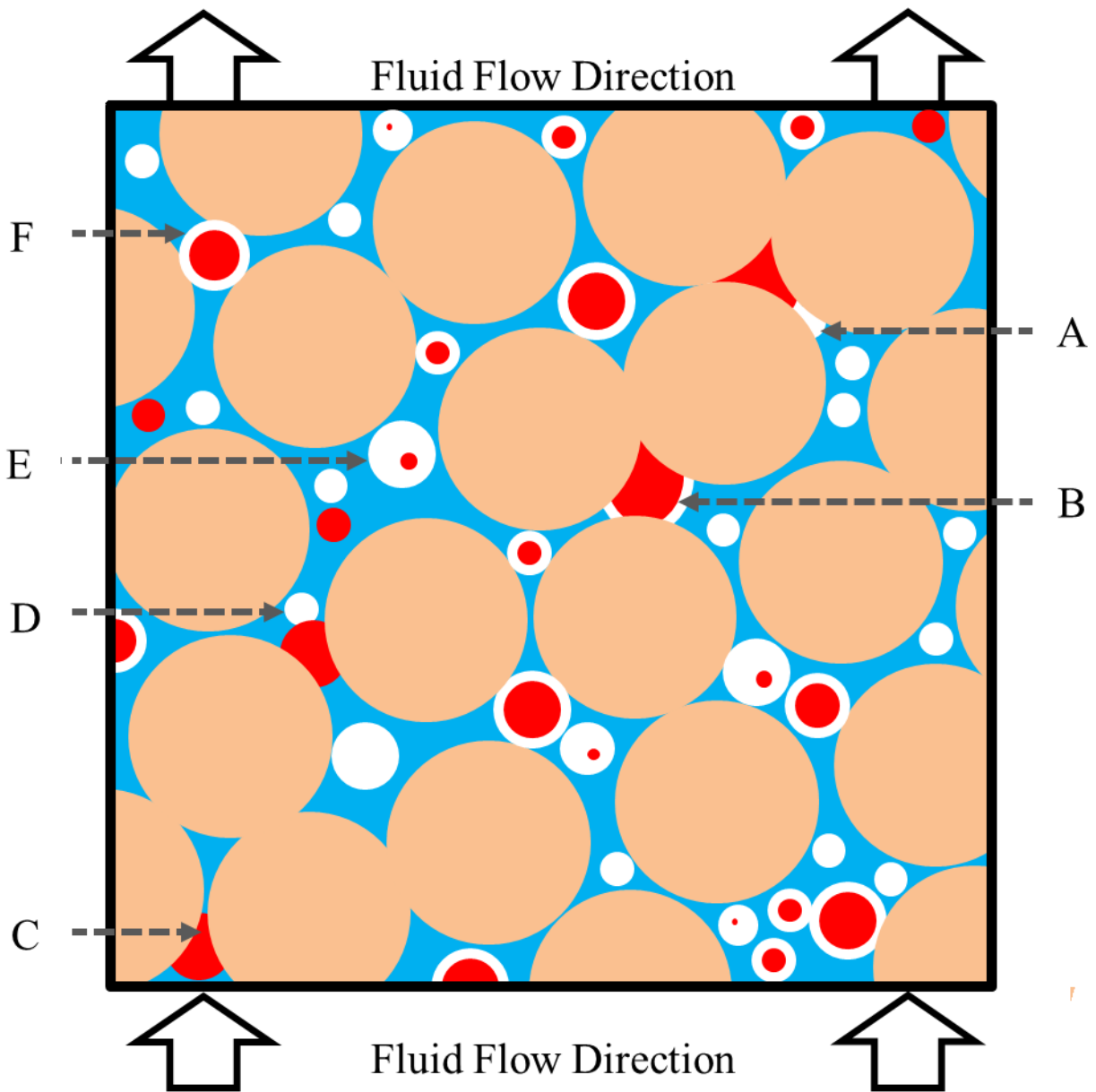
790

791



792

793 Figure 3. Evolution of water, methane gas and methane hydrate saturation during three hydrate  
 794 formation and dissociation cycles in Berea sandstone. The saturations were calculated from the  
 795 changes in pore pressure and temperature (Section 3.1). We used a hydration number of 6.39  
 796 corresponding to 90% cage occupancy (Sloan & Koh, 2007). Note the contracted y-axis scale.  
 797 The first cycle is not shown because the pressure logger malfunctioned. Relative error in  
 798 saturation is less than 0.5%.

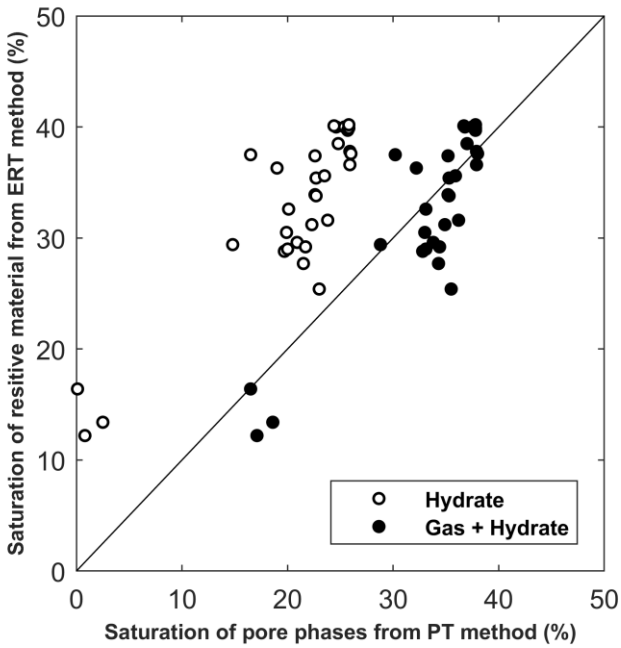


799

800 Figure 4. Conceptual model showing various mechanisms (marked A to F) for co-existence of  
 801 methane gas and hydrate even when methane hydrate stability conditions prevail in the system.  
 802 Red is methane gas, white is hydrate, brown is sand and blue is saline water (brine). A, B: pore  
 803 blocked by hydrate formation. C: capillary pressure of pore not allowing the gas to move through  
 804 it. D: capillary pressure of the pore increased by hydrate formation, not allowing further passage

805 of gas. E: occlusions (unconnected inclusions) of gas within hydrate. F: hydrate film enveloping  
806 the gas bubble.

807



808

809 Figure 5. Total methane gas and methane hydrate saturations (volume percentage of pore space)  
810 from the pressure temperature (PT) method plotted against saturation of all resistive material  
811 deduced from the resistivity (ERT) method. Relative errors in the saturations calculated from the  
812 ERT and PT methods are less than 2% and 0.5%, respectively.